



Title	A nanoindentation study on the room-temperature plasticity in titanium dioxide bicrystals
Author(s)	Janus, Felix; Kinoshita, Ryosuke; Li, Ruqi et al.
Citation	Journal of the American Ceramic Society. 2025, p. e20593
Version Type	VoR
URL	https://hdl.handle.net/11094/102223
rights	© 2025 The Author(s). Journal of the American Ceramic Society published by Wiley Periodicals LLC on behalf of American Ceramic Society.
Note	



The University of Osaka Institutional Knowledge Archive : OUKA

<https://ir.library.osaka-u.ac.jp/>

The University of Osaka

SPECIAL ISSUE ARTICLE

A nanoindentation study on the room-temperature plasticity in titanium dioxide bicrystals

Felix Janus^{1,2} | Ryosuke Kinoshita¹ | Ruoqi Li¹ | Kimitaka Higuchi³ |
Eita Tochigi⁴ | Atsutomo Nakamura¹  | Yan Li¹ 

¹Department of Mechanical Science and Bioengineering, The University of Osaka, Toyonaka, Japan

²Department of Materials and Earth Sciences, Technical University of Darmstadt, Darmstadt, Germany

³Institute of Materials and Systems for Sustainability, Nagoya University, Nagoya, Japan

⁴Institute of Industrial Science, The University of Tokyo, Tokyo, Japan

Correspondence

Atsutomo Nakamura, and Yan Li
Email: a.nakamura.es@osaka-u.ac.jp and li.yan.es@osaka-u.ac.jp

Funding information

Japan Society for the Promotion of Science KAKENHI, Grant/Award Numbers: JP24H00285, JP24K17169, JP22H04960, JP24H00032

Abstract

The increasing demand for manufacturing, processing, and utilizing ceramic materials necessitates a deeper understanding of their mechanical properties, particularly plasticity. In this study, the nanoindentation responses of rutile titanium dioxide (TiO₂) were investigated using bicrystal samples. Two types of TiO₂ bicrystals with symmetric 10° tilt grain boundaries were fabricated by diffusion bonding: one with a (001) tilt grain boundary around the [110] rotation axis, and the other with a (010) tilt grain boundary around the [001] rotation axis. High-resolution transmission electron microscopy observations showed that both bicrystals contained a low-angle grain boundary composed of periodic dislocations. Nanoindentation experiments were conducted in the single-crystal regions to characterize the mechanical properties of rutile TiO₂, as well as near the grain boundary to evaluate its influence on hardness. Nanoindentation results from the single-crystal regions showed that the (001) plane exhibited significantly higher hardness and elastic modulus than the {110} and (100) planes, indicating the anisotropic mechanical behavior of TiO₂. The (010) and (100) planes are two equivalent crystallographic planes in rutile TiO₂, but the (001) plane differs from them. Scanning probe microscopy revealed clear slip traces near the indents without accompanying cracks, indicating that nanoindentation at 5 mN achieved dislocation-mediated plasticity in rutile TiO₂ at room temperature. For nanoindentations on the {110} and (001) planes, plastic deformation was governed by the {101}<10 $\bar{1}$ > slip system, while the (100)[010] slip system dominated the plasticity for nanoindentations on the (100) plane. Nanoindentation experiments near grain boundaries revealed a pronounced hardness peak at the (001) grain boundary, whereas a minor hardening effect was observed at the (010) grain boundary. These findings provide new insights into the room-temperature plasticity, mechanical anisotropy, and grain boundary hardening effects in rutile crystals.

This is an open access article under the terms of the [Creative Commons Attribution-NonCommercial](https://creativecommons.org/licenses/by-nc/4.0/) License, which permits use, distribution and reproduction in any medium, provided the original work is properly cited and is not used for commercial purposes.

© 2025 The Author(s). *Journal of the American Ceramic Society* published by Wiley Periodicals LLC on behalf of American Ceramic Society.

KEYWORDS

grain boundaries, hardness, indentation, plasticity, titanium dioxide

1 | INTRODUCTION

In contrast to metals and metallic alloys, which can undergo extensive plastic deformation, most ceramics are brittle and exhibit little or no plasticity at low-to-moderate temperatures.^{1–3} This brittleness inherently originates from the strong ionic and covalent bonds in ceramics.^{1,4} The complex crystal structure and pronounced anisotropy in many ceramics further restrict their ability to accommodate plastic deformation. Hence, crystal defects, represented by dislocations, have attracted increasing research interest as they play a critical role in determining the mechanical properties of ceramics^{5–7} and have a broad impact on a wide range of functional characteristics.^{8–10}

Nanoindentation has emerged as an effective technique for inducing dislocations into ceramics at room temperature.^{11–15} Under uniaxial compression, most ceramic materials are known to fail prematurely below the elastic strain limit, leaving no opportunity for dislocation glide or nucleation. In contrast, nanoindentation creates a localized, non-uniform high-stress field that can approach the theoretical strength of the material,^{12,14,15} enabling dislocation nucleation, multiplication, and glide within the stressed volume without triggering crack initiation. Furthermore, the high spatial resolution and positional accuracy of nanoindentation promote the investigation of local plasticity, particularly near the grain boundary (GB).^{16–19} When the indenter tip radius and the applied load are reduced, the resulting plastic zone becomes sufficiently small, thereby increasing the proportion of the GB within the stressed volume. Under such conditions, the nanoindentation response is more likely to reflect the characteristics of a single GB. On the other hand, if the plastic zone is too large, the influence of the GB will be masked by the bulk response. Therefore, the impact of a single GB can be effectively investigated by selecting an appropriate combination of indenter tip radius and applied load. For instance, Soer and De Hosson reported a significant hardness peak near a high-angle GB in a Fe-14%Si bicrystal,²⁰ while Nakamura et al. observed negligible hardness changes at the single 20° YSZ GB and $\Sigma 5$ SrTiO₃ GB.¹¹ Nanoindentation has proven to be a powerful tool for studying deformation mechanisms involving dislocations and GBs in ceramics.

Titanium dioxide (TiO₂), widely used in photocatalysis,²¹ solar cells,²² and gas sensors,²³ has mechanical properties that remain insufficiently under-

stood. Previous studies have reported that rutile TiO₂ single crystals were brittle under uniaxial compression at temperatures below 600°C.^{24–26} At elevated temperatures (>600°C), plastic deformation can occur through activation of the {101}<10 $\bar{1}$ > and {110}<001> slip systems. The lack of room-temperature plasticity in rutile TiO₂ has led to a scarcity of subsequent research on its mechanical behavior under ambient conditions. In 2012, Basu et al. investigated the indentation stress-strain responses of TiO₂ at room temperature and performed microscopic postindentation observations.²⁷ However, the high indentation load inevitably caused surface cracks,²⁷ complicating the interpretation of indentation plasticity. More recently, Bishara et al. employed a nanoindentation “pop-in stop” method to locally introduce dislocations into rutile TiO₂ at room temperature without crack formation.²⁸ These dislocations were found to significantly enhance the electrical conductivity of TiO₂,²⁸ demonstrating the important role of defects in modulating functional properties.²⁹ Therefore, investigations into the room-temperature dislocation-based plasticity in TiO₂ are essential for both advancing the fundamental understanding of rutile crystals and unlocking the application potential.

In this study, two types of TiO₂ bicrystals featuring different 10° tilt grain boundaries were fabricated to investigate the nanoindentation responses of rutile TiO₂. The GB structures were characterized using high-resolution transmission electron microscopy (HRTEM). Nanoindentation experiments were conducted at room temperature in the single-crystal regions (far from the GB) and in the GB vicinity, respectively. In the single-crystal regions, nanoindentation experiments were conducted on the {110}, (001), and (100) planes to examine the anisotropic mechanical properties of rutile TiO₂. Scanning probe microscopy (SPM) observations confirmed that no cracks were induced by the room-temperature nanoindentation tests. Furthermore, the nanoindentation plasticity of rutile TiO₂ was governed by the {101}<10 $\bar{1}$ > and (100)[010] slip systems. Nanoindentation tests performed in the GB vicinity showed a pronounced increase in hardness at the (001) GB, while a slight increase in hardness was observed at the (010) GB. These findings enrich the understanding of room-temperature plasticity, anisotropy, and dislocation–GB interactions in rutile ceramics, contributing to optimizing their properties and functionalities through targeted defect engineering.

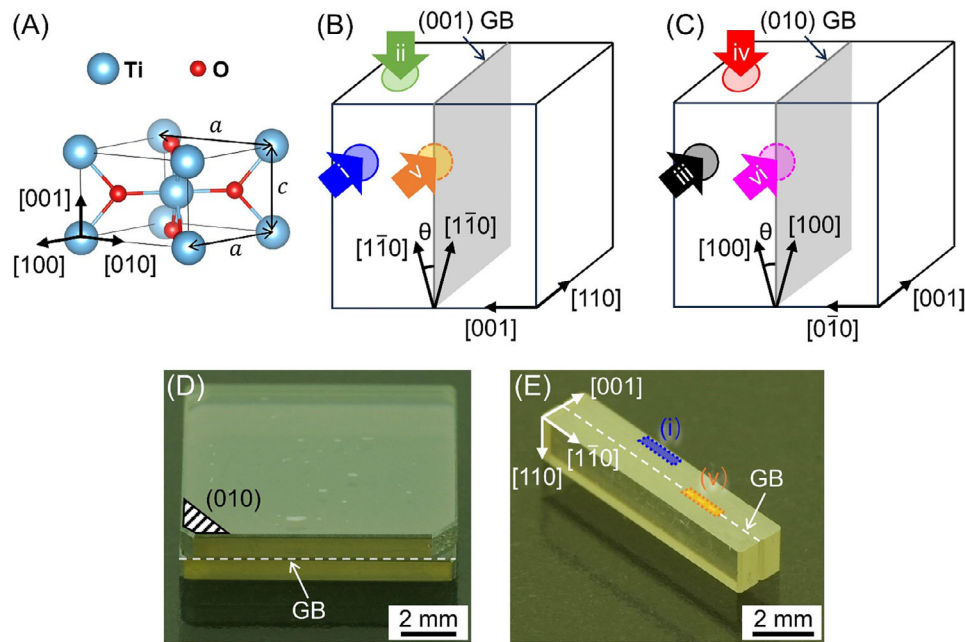


FIGURE 1 (A) The crystal structure of rutile TiO_2 . Schematics of (B) the (001)[110] bicrystal and (C) the (010)[001] bicrystal. The grain boundaries (GBs) are represented by gray quadrangles. Colored arrows indicate conditions: (i) [110], (ii) [110], (iii) [001], and (iv) [100] in the single-crystal region far from the GB; (v) [110]-(001)GB, and (vi) [001]-(010)GB in the GB vicinity. (D) Top view of the (010)[001] bicrystal, with dimensions $10 \text{ mm} \times 10 \text{ mm} \times 2 \text{ mm}$. (E) 45° view of the sample subjected to nanoindentation along the [110] axis, the size of the sample is $10 \text{ mm} \times 2 \text{ mm} \times 2 \text{ mm}$. In (D) and (E), the GB was highlighted by a white dashed line.

2 | EXPERIMENTAL METHODS

2.1 | Sample preparation

The crystal structure of rutile TiO_2 (space ground: $P4_2/mnm$) is displayed in Figure 1A. The lattice constants are $c_{[001]} = 0.296 \text{ nm}$ and $a_{[100]} = a_{[010]} = 0.460 \text{ nm}$.³⁰ The (100) and (010) planes are two equivalent crystallographic planes, whereas the (001) plane differs from them. Two different types of TiO_2 bicrystals were produced by diffusion bonding of single crystal substrates ($10 \text{ mm} \times 10 \text{ mm} \times 1 \text{ mm}$, Shinkosha Co., Ltd.). Both bicrystals had a symmetric 10° tilt GB. For the first bicrystal, the bonding interface, which formed the GB plane, was the (001) plane. As illustrated in Figure 1B, the (001) planes of the two constituent single crystals were rotated in opposite directions by 5° along the [110] axis, resulting in a total 10° tilt GB. The GB is delineated by the gray quadrangle. For the second bicrystal, the GB plane was (010) and the rotation axis was [001], as illustrated in Figure 1C. In the following, the bicrystals will be referred to as (001)[110] and (010)[001]. The diffusion bonding was conducted at 900°C for 5 h, followed by 1100°C for 5 h, under a pressure of approximately 0.1 MPa in air. The camera images of the fabricated bicrystals (001)[110] and (010)[001] are shown in Figure S1 and Figure 1D, respectively.

TABLE 1 Details of the six testing conditions.

Condition	Loading direction	Indentation plane	Indentation region
(i) [110]	[110]	(110)	Single crystal
(ii) [110]	[110] ^a	(110) ^a	Single crystal
(iii) [001]	[001]	(001)	Single crystal
(iv) [100]	[100] ^a	(100) ^a	Single crystal
(v) [110]-(001)GB	[110]	(110)	(001) GB vicinity
(vi) [001]-(010)GB	[001]	(001)	(010) GB vicinity

^aThere is a 5° offset from the crystal orientation or crystal plane.

Six testing conditions were achieved by appropriately selecting the nanoindentation loading direction and region, as listed in Table 1. Taking the (001)[110] bicrystal in Figure 1B as an example, if nanoindentation tests are performed along the [110] axis in a single-crystal region far from the GB, as indicated by the blue arrow (i) in Figure 1B, the results reflect the mechanical properties of the (110) plane. This testing condition is designated as condition (i) [110]. Nanoindentation tests conducted along the [110] axis in a single-crystal region far from the GB, as indicated by the green arrow (ii) in Figure 1B, provide insights into the mechanical responses of the (110) plane. Thus, the condition is labeled as condition (ii) [110]. It should be noted that due to the bicrystal geometry, nanoindentation tests in this case are conducted with a 5° offset from the [110] axis. For

the (100)[001] bicrystal in Figure 1C, conditions (iii) [001] and (iv) [100] were defined analogously, as marked by the black arrow (iii) and red arrow (iv) in Figure 1C.

When nanoindentation tests are performed along the [110] axis in the vicinity of the (001) bicrystal GB, as indicated by the orange arrow (v) in Figure 1B, the results characterize the local mechanical properties of the (110) plane affected by possible dislocation–GB interactions. This condition is termed condition (v) [110]–(001)GB. Similarly, condition (vi) [001]–(010)GB, indicated by the pink arrow (vi) in Figure 1C, is defined to study the local mechanical responses near the (010) bicrystal GB. Bicrystals used in this work, which allow for precise design and control of GB structures,^{31–34} serve as ideal model systems for investigating the effect of GBs on plastic deformation in ceramics.^{11,35}

Nanoindentation experiments under conditions (i) and (v) were conducted on the same sample, as shown in Figure 1E. The bar-shaped sample with the (110) plane as its upper and lower surfaces was cut from the (001)[110] bicrystal. The GB plane (white dashed line) was located in the middle of the sample and perpendicular to the (110) surface. This sample was subjected to nanoindentation tests along the [110] axis, with indentation regions for conditions (i) and (v) indicated by the blue and orange strips, respectively. Samples required for the other testing conditions were also prepared from the bicrystals. All samples were mechanically polished using diamond suspensions with particle sizes of 3 μm and 0.5 μm , followed by chemical mechanical polishing with colloidal silica to ensure sufficient surface flatness. The samples underwent thorough ultrasonic cleaning before nanoindentation tests.

2.2 | Nanoindentation experiments

Nanoindentation tests were conducted in *load-controlled* mode using the instrumented nanoindentation platform ENT-NEXUS (ELIONIX Inc.). A maximum load of 5 mN was applied with a loading rate of 0.5 mN/s, followed by unloading at the same rate after a 0.5-s hold. The spacing between adjacent indentations was set to 10 μm . A diamond Berkovich indenter was used, and the entire setup was maintained at a constant temperature of 30°C. It is noteworthy that all nanoindentation tests were performed in darkness, as light illumination has been shown to significantly impact the dislocation behavior of semiconducting ceramics.^{6,13–15,36}

Nanoindentation experiments under conditions (i)–(iv) were conducted in the single-crystal regions far from GBs, as illustrated in Figure 1B,C. Specifically, 20 indentations were performed for conditions (i) and (iii), and 50 indentations were performed for conditions (ii) and (iv). Under

conditions (v) and (vi), nanoindentation tests were carried out within 5 μm of the GB. For condition (v), the number of indentations per given distance exceeded 30, while for condition (vi), it was 20.

2.3 | Characterization methods

The GBs in the bicrystals were examined using a HRTEM (JEOL JEM-1000K RS) operated at 1 MV. Specimens for HRTEM observation were prepared by a standard technique involving mechanical grinding and Ar^+ ion milling. Before and after the nanoindentation trials, the surface topography was mapped with SPM (SPM-8100FM, Shimadzu). The arithmetic roughness prior to the indentation tests was $R_a \leq 0.2$ nm on all samples, ensuring the flatness required for nanoscale experiments. Postindentation observations were focused on residual indent marks. The slip traces were analyzed to confirm possible activated slip systems. For conditions (v) and (vi), the position and distance of each indent relative to the GB were inspected using a confocal laser microscope (VK-X100 series, Keyence), please refer to the laser optical images in Figure S2.

3 | RESULTS AND DISCUSSION

3.1 | Microstructure of the bicrystals

Figure 2 displays cross-sectional edge-on HRTEM images and the corresponding zone axis diffraction patterns of the (001)[110] and (010)[001] bicrystals. In Figure 2A, the GB is horizontally located at the center of the image, and periodic bright regions are visible between the two rotated single crystals. The perfect single-crystal regions in the upper and lower sections, separated by the bright regions at the boundary, are continuous within their respective areas. In low-angle GBs, it is well established that GB structures can be described by a periodic array of dislocations.³⁵ The positions of the GB dislocations, which correspond to the bright regions in Figure 2A, are indicated by white arrows. The average distance between two dislocations is $L_1 = 1.72$ nm. In Figure 2B, the corresponding diffraction pattern is displayed. All reflections appear in pairs with an angular distance of approximately 10° , which is equal to the designed tilt angle. The diffraction patterns also did not indicate the formation of any secondary phase. It can be thus said that the bonding of the (001)[110] bicrystal's GB has been achieved at the atomic level.

Figure 2C displays the GB region of the (010)[001] bicrystal. At the position of the GB, white arrows mark the

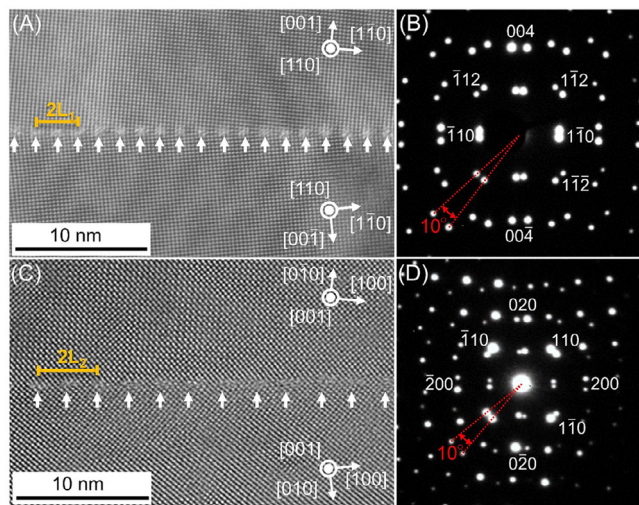


FIGURE 2 Low-magnification high-resolution transmission electron microscopy (HRTEM) images to show the bonding conditions of the grain boundaries (GBs) and corresponding zone diffraction patterns. For (001)[110] bicrystal: (A) the HRTEM image, (B) the [110] zone axis diffraction pattern. For (010)[001] bicrystal: (C) the HRTEM image, (D) the [001] zone axis diffraction pattern.

periodic array of blurry regions caused by a misalignment of the atomic arrangement. The observed regions are related to structural defects, specifically dislocations, at the GB. The average distance between two dislocations is $L_2 = 2.45$ nm. The GB bonding is good and shows no other defects. In the diffraction pattern in Figure 2D, the reflections are paired and their angular distance is on average 10° . The angular distance of the diffraction spots and rotation of the single crystals both indicate that the intended bicrystal geometry was achieved.

The interval of boundary dislocations is related to the misorientation angle between adjacent single crystals and the Burgers vector of GB dislocations. According to Frank's formula,³⁷ the spacing between adjacent boundary dislocations L in a tilt GB can be expressed by:

$$L = \frac{b}{\sin(2\theta)}, \quad (1)$$

where b is the magnitude of the Burgers vector of the boundary dislocation, and 2θ is the total tilt angle. Substituting the interval and tilt angle from the HRTEM image in Figure 2A,C into Frank's formula yields Burgers vector magnitudes of $b_1 = 0.299$ nm in the (001)[110] bicrystal, and $b_2 = 0.425$ nm in the (010)[001] bicrystal. The lattice constants for rutile TiO_2 are $c_{[001]} = 0.296$ nm and $a_{[100]} = a_{[010]} = 0.460$ nm.³⁰ The approximation between the calculated Burgers vector magnitudes and the lattice constants suggests that dislocations with a Burgers vector of $b_1 = [001]$ were introduced at the (001)[110] bicrystal GB,

TABLE 2 Hardness and elastic modulus values under conditions (i)–(iv).

Condition	Hardness [GPa]	Elastic modulus [GPa]
(i) [110]	12.38 ± 0.16	252.95 ± 5.42
(ii) $[1\bar{1}0]$	12.34 ± 0.16	255.11 ± 4.91
(iii) [001]	13.26 ± 0.25	328.81 ± 10.91
(iv) [100]	12.20 ± 0.16	250.29 ± 5.96

while dislocations with a Burgers vector of $b_2 = [010]$ were introduced at the (010)[001] bicrystal GB.

3.2 | Anisotropic mechanical properties

Figure 3A displays the representative load-depth curves for the nanoindentation tests conducted under conditions (i)–(iv). The curves corresponding to conditions (i), (ii), (iii), and (iv) are depicted as blue, green, black, and red solid lines, respectively. As explained in Section 2.1, the results obtained in conditions (i), (ii), (iii), and (iv) reflect the mechanical properties of the (110) plane, the $(1\bar{1}0)$ plane, the (001) plane, and the (100) plane, respectively. Under an indentation load of 5 mN, the indentation depth at the peak load in condition (iii) is the smallest at 120 nm, whereas for the other three conditions, the depth at the peak load is approximately 130 nm.

Nanoindentation hardness (H) and elastic modulus (E) values were extracted from the load–depth curves using the Oliver–Pharr method.³⁸ The measurement results for different conditions are summarized in Figure 3B and Table 2. The average values and standard deviations for conditions (i), (ii), (iii), and (iv) are represented by blue, green, black, and red scatters with corresponding error bars, respectively. The average values for conditions (i) and (iii) were calculated from 20 data points, and 50 data points were used for conditions (ii) and (iv). The average hardness values for the (110), $(1\bar{1}0)$, (001), and (100) planes are 12.38, 12.34, 13.26, 12.20 GPa, respectively. The standard deviation of hardness is less than 2% of the average, demonstrating the high reproducibility of the obtained data. For the TiO_2 (110) plane, the measured hardness value agrees with the nanoindentation hardness reported by Kurosaki et al.³⁹ Notably, the hardness of the (001) plane is significantly higher than the other three planes. This trend is consistent with the observations by Basu et al.²⁷ The average elastic modulus values are 252.95 GPa for the (110) plane, 255.11 GPa for the $(1\bar{1}0)$ plane, 328.81 GPa for the (001) plane, and 250.29 GPa for the (100) plane. The elastic modulus for the (001) plane is approximately 30% higher than that of the other three planes. The standard deviation of elastic modulus is less than 4% of the average. The elastic anisotropy is evident, with the highest modulus observed

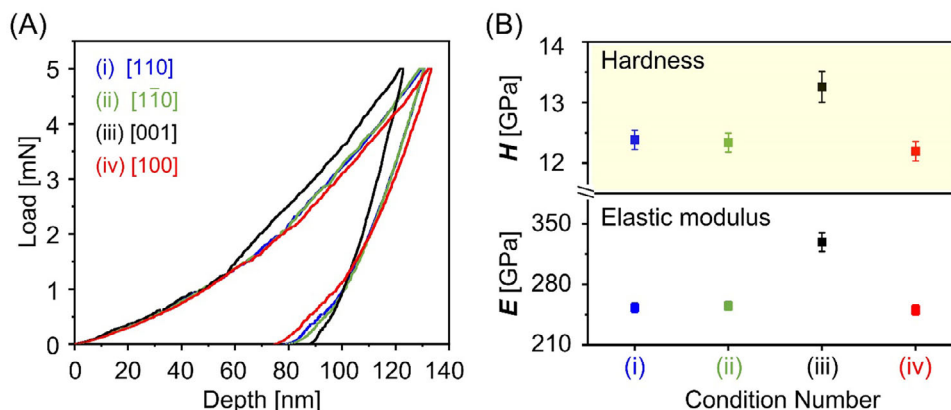


FIGURE 3 (A) Representative nanoindentation load-depth curves under conditions (i) [110], (ii) [110], (iii) [001], and (iv) [100]. (B) Nanoindentation hardness (H) and elastic modulus (E) values measured in nanoindentation experiments under conditions (i)–(iv).

for the (001) plane. The high elastic modulus of the (001) plane partly contributes to its high hardness. In addition, the (110) plane in condition (i) and the (110) plane are two equivalent {110} crystal planes. The nearly identical modulus and hardness values for conditions (i) and (ii) demonstrate the negligible influence of the 5° offset from the (110) plane in condition (ii) on the measurement.

3.3 | Slip system analysis

SPM was used to examine the topography near the residual indent pits and to identify the possible slip systems activated by nanoindentation. For conditions (i) to (iv), the SPM gradient topography images of the indent pits are presented in Figure 4, with the corresponding SPM height images shown in Figure S3. As seen in Figure 4A–D, no detectable cracks were observed under any of the four conditions, indicating that nanoindentation at 5 mN in this study successfully induced local plasticity in rutile TiO₂ at room temperature. The side length of the residual indentation triangle is less than 0.9 μm, demonstrating that the 10 μm spacing is sufficient to avoid interactions between adjacent indentations. The SPM images in Figure 4A–D show no evidence of pile-up or sink-in around the residual indentations, contrasting with nanoindentation behaviors in most metals and alloys.^{40,41} Such a feature is increasingly recognized in ceramics with limited room-temperature plasticity.^{13,15} Moreover, clear line features around the indent in Figure 4A–D suggest the occurrence of dislocation-mediated plasticity. The likely most active slip planes for each condition are illustrated in schematics beneath the SPM images. The color coding in Figure 3 is maintained in Figure 4 for consistency.

Figure 4A,B shows the SPM images corresponding to conditions (i) [110] and (ii) [110], respectively. In both images, the surfaced slip traces align with the rhombus-

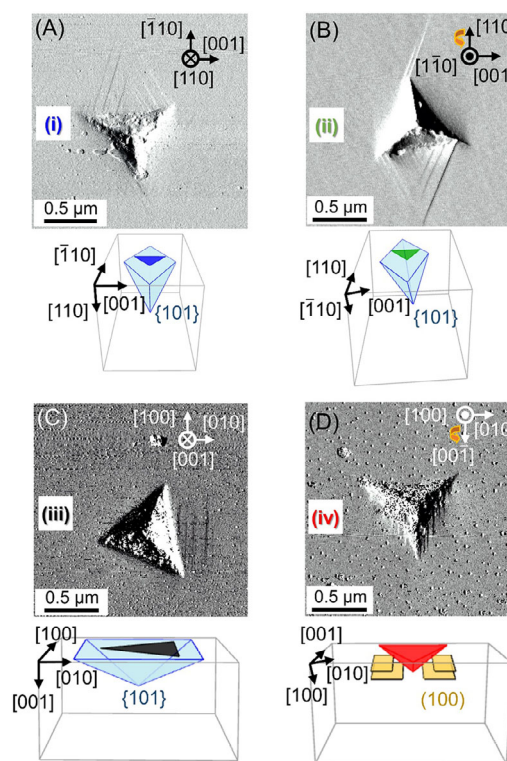


FIGURE 4 Topography gradient scanning probe microscopy (SPM) images of indentation pits introduced by 5 mN load nanoindentation corresponding to (A) (i) [110], (B) (ii) [110], (C) (iii) [001], and (D) (iv) [100] with a cartesian coordinate system and rotation indicating arrow (orange), and schematic 3D models of the projection of the {101}<101> (light blue) and (100)[010] slip system planes (orange) below the nanoindent pits (triangles). The black and white contrast in SPM images symbolizes a change in height signal.

shaped projection of the {101} planes on the surface. Thus, the mainly activated slip system under both conditions is the {101}<101> slip system. The two indentation directions, (i) [110] and (ii) [110], are nearly equivalent in the rutile crystal structure. This equivalence is reflected not

only in the nearly identical hardness and modulus values discussed in Section 3.2, but also in the activation of the same slip system.

Figure 4C,D displays the SPM images for conditions (iii) [001], and (iv) [100], respectively. In Figure 4C, slip traces are mainly oriented parallel to the [100] axis. In an additional SPM image shown in Figure S4, slip traces parallel to the [010] axis also faintly emerged. The best matching slip system is hence the $\{101\}\langle 10\bar{1}\rangle$ slip system. It is noteworthy that the load-depth curve for the [001] nanoindentation in Figure 3A (represented by the black line) exhibits a slope change at a depth of approximately 55 nm. The increase in slope suggests a hardening effect, which may be related to the motion and interaction of dislocations associated with the four equivalent slip systems. For condition (iv) [100], no slip traces are visible outside the indent pit in Figure 4D. However, traces parallel to the [001] axis appear inside the pit. According to Basu et al.,²⁷ such a pattern does not coincide with the $\{101\}\langle 10\bar{1}\rangle$ but rather with the (100)[010] slip system.

Previously, Basu et al. reported that indentation on the (001) plane in the 80–150 mN range would activate four equivalent $\{101\}\langle 10\bar{1}\rangle$ slip systems, contributing to the high hardness of this orientation.²⁷ Meanwhile, indentation on the (100) plane in the 80–150 mN range could activate both $\{101\}\langle 10\bar{1}\rangle$ and (100)[010] slip systems.²⁷ Our experiments, conducted at a much lower load of 5 mN, capture the early stages of plastic deformation. For the (001) plane, the SPM results in Figure 4C and Figure S4 confirmed the activation of the $\{101\}\langle 10\bar{1}\rangle$ slip system, consistent with the high-load indentation tests by Basu et al. However, observations on the (100) plane revealed the presence of (100)[010] slip and absence of the $\{101\}\langle 10\bar{1}\rangle$ slip, suggesting the significant role of the (100)[010] slip system in the early-stage plastic deformation of rutile (100) TiO_2 . Hirthe and Brittain proposed the activation of (100)[010] slip system by observations of slip traces and slip lines in their etch-pit study.⁴² Hence, it is plausible that the (100)[010] dislocations can be predominantly activated in the low-load indentation along the [001] axis.

3.4 | Effects of GB on nanoindentation hardness

Figure 5 presents the nanoindentation hardness plots as a function of the distance from the GB for conditions (v) [110]-(001)GB and (vi) [001]-(010)GB. The number of indents per given distance N is > 30 for condition (v), and $N = 20$ for condition (vi). For ease of comparison, the hardness value for conditions (i) [110] and (iii) [001] obtained in the single-crystal regions are also included in

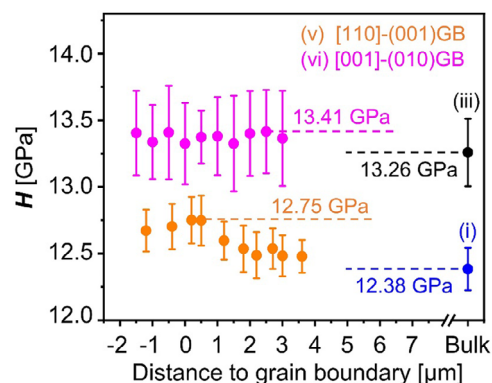


FIGURE 5 Nanoindentation hardness versus grain boundary (GB) distance diagram under conditions (v) [110]-(001)GB and (vi) [001]-(010)GB. The number of indents per given distance N is > 30 for condition (v), and $N = 20$ for condition (vi).

Figure 5, represented by the blue and black scatter points, respectively.

For condition (v) [110]-(001)GB, depicted by the orange data points in Figure 5, the hardness gradually increases as the GB is approached, reaching a peak value of 12.75 ± 0.17 GPa at nearly zero distance. After crossing the GB, the hardness decreases again. The hardness measured far from the GB, obtained under condition (i), is 12.38 ± 0.16 GPa. The hardness at the GB is approximately 3% higher than that in the single-crystal region. Given the high repeatability and small standard deviation of the nanoindentation hardness tests, the GB hardening effect is statistically significant. It is worth noting that the asymmetry in hardness values around zero distance may arise from the non-symmetric stress field induced by the pyramidal Berkovich indenter.⁴³ This asymmetry was also observed in previous research using a Berkovich indenter to map nanoindentation hardness crossing the GB.^{20,44}

For condition (vi) [001]-(010)GB, represented by the pink data points in Figure 5, the hardness exhibits a minor increase towards the GB. The maximum hardness value near the GB is 13.41 ± 0.35 GPa, which is slightly higher than the hardness measured under condition (iii) without any GB influence (13.26 ± 0.25 GPa). The minor change in hardness suggests that the hardening effect of the (100) GB is relatively limited.

In ceramics, the low-angle tilt GB can act as an obstacle to impede dislocation motion, leading to increased hardness in close proximity to the GB. Dislocation pileups may occur at the GB.^{11,35} In addition, nanoindentation-induced dislocations can interact with the GB dislocations.³⁵ Kondo et al. conducted in-situ TEM nanoindentation near a single low-angle tilt GB in the SrTiO_3 bicrystal.³⁵ Their observations revealed that the intersection of indentation-induced screw dislocations with GB edge dislocations resulted in

the formation of kinks on the screw dislocations and jogs on the GB dislocations, thereby hindering dislocation glide across the GB.³⁵

In conditions (v) and (vi), the activated slip system by nanoindentation is the same as that in conditions (i) and (iii), respectively. As shown in Figure 4A,C, the $\{101\}\langle 10\bar{1}\rangle$ slip system was activated in both conditions. However, the interaction of indentation-induced dislocations with different GBs shall result in different hardening effects. In condition (i), the (001) GB consists of dislocations with a Burgers vector of $b_1 = [001]$, while in condition (ii), dislocations with a Burgers vector of $b_2 = [010]$ were present at the (010) GB. When indentation-induced dislocations are to cross the GB, the Burgers vector have to undergo rotation.^{30,35} Since the Burgers vector must be conserved within a crystal, this rotation inevitably leaves a residual dislocation at the GB.⁴⁵ The formation of the residual dislocation strongly depends on the nature of the existing GB dislocations, which may explain why the hardening effect in condition (v) is more significant than that in condition (vi). Furthermore, in condition (v), the spacing between GB dislocations is only 1.72 nm, whereas on the (010) GB in condition (vi), the spacing is 2.45 nm. The higher dislocation density in condition (v) may also contribute to the more pronounced GB hardening effect. More delicate characterizations, including cross-sectional TEM observations, will be needed to further elucidate the GB–dislocation interactions underlying the observed GB hardening effect.

In this study, the nanoindentation experiments were conducted with a peak load of only 5 mN. Such a low load not only allows for the introduction of local plasticity without crack formation but also creates a suitable plastic zone, enabling the examination of the GB hardening effect in rutile TiO_2 . Due to the low load, the stress field beneath the indenter remains confined to a small deformation volume. A higher load would generate a higher stress field and a larger deformation volume, making it difficult to resolve localized hardness variations affected by the GB. In addition, the characteristics of GB itself plays a crucial role in determining the GB hardening effect in ceramics. For instance, Nakamura et al. detected negligible hardness changes near single GBs of Y_2O_3 -stabilized ZrO_2 bicrystal and SrTiO_3 bicrystal,¹¹ while Lian et al. reported a hardness decrease at the F-YSZ GB.⁴⁴

4 | CONCLUSION

The room-temperature mechanical properties of rutile titanium dioxide were investigated using bicrystal fabrication, nanoindentation technique and SPM observations. Two types of TiO_2 bicrystals with symmetric 10° tilt GBs were fabricated using a diffusion bonding method: one with a

(001) tilt GB around the $[110]$ rotation axis, and the other with a (010) tilt GB around the $[001]$ rotation axis. HRTEM observations revealed that the symmetric 10° tilt GBs consist of periodically arranged dislocation lines, and the bonding at the GBs was intact. By designing the nanoindentation loading direction and region, we measured the mechanical properties of TiO_2 single crystals, and also evaluated the GB effect on nanoindentation responses. The hardness values for the $\{110\}$, (001), and (100) planes were measured as 12.38 ± 0.16 GPa, 13.26 ± 0.25 GPa, and 12.20 ± 0.16 GPa, respectively. The elastic modulus values for the $\{110\}$, (001), and (100) planes were 252.95 ± 5.42 GPa, 328.81 ± 10.91 GPa, and 250.29 ± 5.96 GPa, respectively. The results demonstrated anisotropy in the mechanical properties of rutile TiO_2 , with the (001) plane exhibiting the highest hardness and elastic modulus. Moreover, nanoindentation at 5 mN successfully induced local plasticity in rutile TiO_2 at room temperature without crack initiation. SPM observations showed that the $\{101\}\langle 10\bar{1}\rangle$ slip system was predominately activated during indentations on the $\{110\}$ plane and the (001) plane, while the (100)[010] slip system was activated during indentations on the (100) plane. The bicrystal GB was found to influence the measured hardness values: a significant increase in hardness, approximately 3%, was observed at the (001) GB when indenting along the $[110]$ axis. However, only a minor hardening effect was detected at the (010) GB when indenting along the $[001]$ axis.

ACKNOWLEDGMENTS

This research is funded by Japan Society for the Promotion of Science KAKENHI Grant Numbers JP24H00285, JP24K17169, JP22H04960, JP24H00032. The authors acknowledge the Research Center for Ultra-High Voltage Electron Microscopy at Nagoya University. The authors thank Adrian Scheer for conducting the initial test trials and paving the road to this investigation, Shuhei Koga for helpful instructions about bicrystal fabrication, and Anna Takagi for assistance in HRTEM image analysis.

ORCID

Atsutomo Nakamura  <https://orcid.org/0000-0002-4324-1512>

Yan Li  <https://orcid.org/0000-0002-9274-2516>

REFERENCES

- Callister Jr WD, Rethwisch DG. Materials science and engineering: an introduction. New York: John Wiley & Sons; 2020.
- Li Y, Liu X, Zhang P, Han Y, Huang M, Wan C. Theoretical insights into the Peierls plasticity in SrTiO_3 ceramics via dislocation remodelling. *Nat Commun*. 2022;13(1):1–10.
- Li J, Cho J, Ding J, Charalambous H, Xue S, Wang H, et al. Nanoscale stacking fault–assisted room temperature plasticity in flash-sintered TiO_2 . *Sci Adv*. 2019;5(9):eaaw5519.

4. Zhang J, Liu G, Cui W, Ge Y, Du S, Gao Y, et al. Plastic deformation in silicon nitride ceramics via bond switching at coherent interfaces. *Science*. 2022;378(D):371–76.
5. Dong LR, Zhang J, Li YZ, Gao YX, Wang M, Huang MX, et al. Borrowed dislocations for ductility in ceramics. *Science*. 2024;385(6707):422–27.
6. Oshima Y, Nakamura A, Matsunaga K. Extraordinary plasticity of an inorganic semiconductor in darkness. *Science*. 2018;360(6390):772–74.
7. Porz L, Klomp AJ, Fang X, Li N, Yildirim C, Detlefs C, et al. Dislocation-toughened ceramics. *Mater Horizons*. 2021;8(5):1528–37.
8. Nakamura A, Matsunaga K, Tohma J, Yamamoto T, Ikuhara Y. Conducting nanowires in insulating ceramics. *Nat Mater*. 2003;2(7):453–56.
9. Fang X, Nakamura A, Rödel J. Deform to perform: dislocation-tuned properties of ceramics. *ACerS Bull*. 2023;102(5):24–29.
10. Porz L, Frömling T, Nakamura A, Li N, Maruyama R, Matsunaga K, et al. Conceptual framework for dislocation-modified conductivity in oxide ceramics deconvoluting mesoscopic structure, core, and space charge exemplified for SrTiO_3 . *ACS Nano*. 2021;15(6):9355–67.
11. Nakamura R, Masuda H, Yoshida H. Nanoindentation responses near single grain boundaries in oxide ceramics. *J Am Ceram Soc*. 2023;106(3):2061–72.
12. Masuda H, Morita K, Ohmura T. Nanoindentation-induced plasticity in cubic zirconia up to 500°C. *Acta Mater*. 2020;184:59–68.
13. Nakamura A, Fang X, Matsubara A, Tochigi E, Oshima Y, Saito T, et al. Photoindentation: a new route to understanding dislocation behavior in light. *Nano Lett*. 2021;21(5):1962–67.
14. Li Y, Fang X, Tochigi E, Oshima Y, Hoshino S, Tanaka T, et al. Shedding new light on the dislocation-mediated plasticity in wurtzite ZnO single crystals by photoindentation. *J Mater Sci Technol*. 2023;156:206–16.
15. Oguri H, Li Y, Tochigi E, Fang X, Tanigaki K, Ogura Y, et al. Bringing the photoplastic effect in ZnO to light: a photoindentation study on pyramidal slip. *J Eur Ceram Soc*. 2024;44(2):1301–5.
16. Javaid F, Pouriaeyvali H, Durst K. Dislocation–grain boundary interactions: recent advances on the underlying mechanisms studied via nanoindentation testing. *J Mater Res*. 2021;36(12):2545–57.
17. Avadanii D, Hansen L, Marquardt K, Wallis D, Ohl M, Wilkinson A. The role of grain boundaries in low-temperature plasticity of olivine revealed by nanoindentation. *J Geophys Res Solid Earth*. 2023;128(8):e2023JB026763.
18. Kalidindi SR, Vachhani SJ. Mechanical characterization of grain boundaries using nanoindentation. *Curr Opin Solid State Mater Sci*. 2014;18(4):196–204.
19. Wo PC, Ngan AHW. Investigation of slip transmission behavior across grain boundaries in polycrystalline Ni_3Al using nanoindentation. *J Mater Res*. 2004;19(1):189–201.
20. Soer WA, De Hosson JTM. Detection of grain-boundary resistance to slip transfer using nanoindentation. *Mater Lett*. 2005;59:3192–95.
21. Huang H, Zhang T, Cai X, Guo Z, Fan S, Zhang Y, et al. In situ one-pot synthesis of C-decorated and Cl-doped sea-urchin-like rutile titanium dioxide with highly efficient visible-light photocatalytic activity. *ACS Appl Mater Interfaces*. 2021;13(50):60337–50.
22. Kavan L, Vlckova Zivcova Z, Zlamalova M, Zakeeruddin SM, Grätzel M. Electron-selective layers for dye-sensitized solar cells based on TiO_2 and SnO_2 . *J Phys Chem C*. 2020;124(12):6512–21.
23. Zhao J, Wang H, Cai Y, Zhao J, Gao Z, Song YY. The challenges and opportunities for TiO_2 nanostructures in gas sensing. *ACS Sensors*. 2024;9(4):1644–55.
24. Ashbee KHG, Smallman RE. Stress-strain behavior of titanium dioxide (Rutile) single crystals. *J Am Ceram Soc*. 1963;46(5):211–14.
25. Ashbee KHG, Smallman RE. The fracture of titanium dioxide single crystals with particular reference to non-stoichiometry. *Phys Status Solidi*. 1964;4:289–98.
26. Takeuchi S, Hashimoto T. Deformation mechanisms in titanium dioxide single crystals. *J Mater Sci*. 1990;25(1):417–23.
27. Basu S, Elshrief OA, Coward R, Anasori B, Barsoum MW. Microscale deformation of (001) and (100) rutile single crystals under spherical nanoindentation. *J Mater Res*. 2012;27(1):53–63.
28. Bishara H, Tsybenko H, Nandy S, Muhammad QK, Frömling T, Fang X, et al. Dislocation-enhanced electrical conductivity in rutile TiO_2 accessed by room-temperature nanoindentation. *Scr Mater*. 2022;212:114543.
29. Muhammad QK, Porz L, Nakamura A, Matsunaga K, Rohnke M, Janek J, et al. Donor and acceptor-like self-doping by mechanically induced dislocations in bulk TiO_2 . *Nano Energy*. 2021;85:105944.
30. Baur WH. Über die verfeinerung der Kristallstrukturbestimmung einiger vertreter des rutiltyps: TiO_2 , SnO_2 , GeO_2 und MgF_2 . *Acta Crystallogr*. 1956;9(6):515–20.
31. Ikuhara Y, Nishimura H, Nakamura A, Matsunaga K, Yamamoto T, Lagerlöf PKD. Dislocation structures of low-angle and near- $\Sigma 3$ grain boundaries in alumina bicrystals. *J Am Ceram Soc*. 2003;86(4):595–602.
32. Nakamura A, Tochigi E, Shibata N, Yamamoto T, Ikuhara Y. Structure and configuration of boundary dislocations on low angle tilt grain boundaries in alumina. *Mater Trans*. 2009;50(5):1008–14.
33. Furushima Y, Nakamura A, Tochigi E, Ikuhara Y, Toyoura K, Matsunaga K. Dislocation structures and electrical conduction properties of low angle tilt grain boundaries in LiNbO_3 . *J Appl Phys*. 2016;120(14):142107.
34. Furushima Y, Arakawa Y, Nakamura A, Tochigi E, Matsunaga K. Nonstoichiometric [012] dislocation in strontium titanate. *Acta Mater*. 2017;135:103–11.
35. Kondo S, Mitsuma T, Shibata N, Ikuhara Y. Direct observation of individual dislocation interaction processes with grain boundaries. *Sci Adv*. 2016;2(11):e1501926.
36. Oguri H, Li Y, Nakamura A. A nanoindentation approach for unveiling the photoplastic effects by a “light switch”: a case study on ZnO. *J Am Ceram Soc*. 2024;108(6):e20338.
37. Frank FC. LXXXIII. Crystal dislocations.—Elementary concepts and definitions. London Edinburgh Dublin Philos Mag J Sci. 1951;42(331):809–19.
38. Oliver WC, Pharr GM. An improved technique for determining hardness and elastic modulus using load and displacement sensing indentation experiments. *J Mater Res*. 1992;7(6):1564–83.

39. Kurosaki K, Setoyama D, Matsunaga J, Yamanaka S. Nanoindentation tests for TiO₂, MgO, and YSZ single crystals. *J Alloys Compd.* 2005;386(1–2):261–64.
40. Muthupandi G, Lim KR, Na YS, Park J, Lee D, Kim H, et al. Pile-up and sink-in nanoindentation behaviors in AlCoCrFeNi multi-phase high entropy alloy. *Mater Sci Eng A.* 2017;696:146–54.
41. Wang Y, Raabe D, Klüber C, Roters F. Orientation dependence of nanoindentation pile-up patterns and of nanoindentation microtextures in copper single crystals. *Acta Mater.* 2004;52(8):2229–38.
42. Hirthe WM, Brittain JO. Dislocations in rutile as revealed by the etch-pit technique. *J Am Ceram Soc.* 1962;45(11):546–54.
43. Larsson P-L, Giannakopoulos AE, Soderlund E, Rowcliffe DJ, Vestergaard R. Analysis of Berkovich indentation. *Int J Solids Struct.* 1996;33(2):221–48.
44. Lian J, Garay JE, Wang J. Grain size and grain boundary effects on the mechanical behavior of fully stabilized zirconia investigated by nanoindentation. *Scr Mater.* 2007;56(12):1095–98.
45. Lim LC, Raj R. Continuity of slip screw and mixed crystal dislocations across bicrystals of nickel at 573 K. *Acta Metall.* 1985;33(8):1577–83.

SUPPORTING INFORMATION

Additional supporting information can be found online in the Supporting Information section at the end of this article.

How to cite this article: Janus F, Kinoshita R, Li R, Higuchi K, Tochigi E, Nakamura A, et al. A nanoindentation study on the room-temperature plasticity in titanium dioxide bicrystals. *J Am Ceram Soc.* 2025;e20593.

<https://doi.org/10.1111/jace.20593>